The impact of sea-ice drift and ocean circulation on dispersal of toothfish eggs and juveniles in the Ross Sea and Amundsen Sea

Erik Behrens[1], Matt Pinkerton[1], Steve Parker[1], Graham Rickard[1], Charine Collins[1]

[1] National Institute of Water and Atmospheric Research, 301 Evans Bay Parade, Hataitai, Wellington 6021, New Zealand

Corresponding author: Erik Behrens, erik.behrens@niwa.co.nz

Key Points:

- Particles drift from the northern Ross Sea to the continental shelf break as part of the Ross Gyre circulation
- Particles which drift with sea-ice have a 70% lower success rate than purely ocean advected particles, but reach the shelf break earlier
- Sea-ice drift during the second winter, in the eastern Ross Sea, carries many particles away from the shelf region

Abstract:

Knowledge about the early life history of Antarctic toothfish (*Dissostichus mawsoni*) is still incomplete, particularly on the spatial and temporal extent of spawning and the subsequent transport of eggs and juveniles from the offshore spawning areas to the continental shelf. This study used a high-resolution hydrodynamic model to investigate the impact of ocean circulation and sea-ice drift on the dispersal of eggs and juvenile Antarctic toothfish. The virtual eggs were released on seamounts of the Pacific-Antarctic ridge in the northern Ross Sea and advected using hydrodynamical model data. Particles were seeded annually over a 14-year period (2002 to 2016) and tracked for three years after release. Spawning success was evaluated based on the number of juveniles that reached known coastal recruitment areas, in the eastern Ross and Amundsen Sea, within three years. Observations show that juveniles (50-100 cm size class) are abundant on the shelf and slope of the Ross and Amundsen Seas. Sensitivities to certain juvenile behaviours were explored and showed that spawning success was reduced by around 70% if juveniles drifted with sea-ice during the second winter season as this carried them into the open ocean away from the shelf region. Spawning success increased during the second winter season if juveniles were entrained in the Ross Gyre circulation or if they actively swam towards the shelf. These modelling results suggest that the ecological advantage of sea-ice association in the early life cycle of toothfish diminishes as they grow, promoting a behaviour change during their second winter.

Plain abstract:

Antarctic toothfish is a large, commercially harvested, fish which is found around Antarctica. These fish lay buoyant eggs in the water column during winter season. Spawning locations in the Ross Sea have been identified around seamounts in the northern part. After spawning the eggs drift to the surface where they encounter sea-ice. Sea-ice drift controls the egg dispersal until the eggs hatch. After hatching they juvenile fish find their way from the Northern Ross Sea to the shelf break in the eastern Ross and Amundsen Sea within 2 to 3 years. In this study we investigate how ocean currents and sea-ice drift influences their journey from the spawning regions to the shelf break using data from high-resolution ocean model in combination with Lagrangian particles tracking. Simulations

with different behaviours reveal that their spawning success is around 70% lower if juveniles would continue to drift with sea-ice instead with the ocean circulation after they hatch. Particular the sea-ice drift during the second winter season carries many juveniles into the open ocean, away from the shelf break. This modelling study suggest that the advantage of sea-ice in the early life stage, providing a shelter and a source of food, reduces with time.

1. Introduction

Antarctic toothfish (*Dissostichus mawsoni*), a notothenioid species endemic to the seas around Antarctica, spawns on bathymetric features in the northern Ross Sea region (S. Hanchet et al., 2015; S. M. Hanchet et al., 2008; S. J. Parker et al., 2019). Spawning has been observed on seamount features at the sea-ice edge in July (S. J. Parker et al., 2019) and was observed to be completed by late August (S. Parker & Di Blasi, 2020). However, much of the adult population is likely further south and under sea-ice during winter. Gonadosomatic index analysis of male and female toothfish suggest that spawning is likely to occur on the hills, banks and ridges north of 70°S where large adults dominate catches (S. M. Hanchet et al., 2008; S. J. Parker et al., 2019). The exact geographic distribution of depths of spawning of *D. mawsoni* is still unknown. Based on the observations from the Ross and Amundsen Sea, and from the South Sandwich Islands, *D. mawsoni* likely spawns in the Ross Sea region at depths of 1000–2000 m (S. Parker & Di Blasi, 2020; S. J. Parker et al., 2019; Roberts, 2012).

The incubation time of *D. mawsoni* eggs as well as the period of passive drift is also not known, largely due to the lack of appropriate times of and locations of plankton samples. Nevertheless, hatching dates for *D. mawsoni* were estimated (La Mesa, 2007) by counting micro-increments between presumed hatching checks and first-feeding checks identified in the core region of sagittal otoliths from juvenile specimens collected around the South Shetland Islands. Using this technique, it was estimated that hatching of *D. mawsoni* eggs takes place between November and February with a peak in December. Combined with information from *D. eleginoides*, a winter spawning period followed by a 3 month incubation and hatching in early spring is likely in the Ross Sea and Amundsen Sea regions (S. M. Hanchet et al., 2008; S. J. Parker et al., 2019). Based on the lack of demersal juveniles smaller than 30 cm being found by bottom longlining in the region, it was hypothesized that *D. mawsoni* juveniles are likely to spend more than a year living in the plankton (S. M. Hanchet et al., 2008). It is likely that swimming abilities of larval and juvenile toothfish would increase during this period (S. M. Hanchet et al., 2008).

Based on a combination of biological data, spatial distribution data and Lagrangian particle tracking using hydrodynamical data from Hi-GEM (Shaffrey et al., 2009), it was hypothesized that adult Antarctic toothfish move northwards from the Ross Sea to spawn on the banks and ridges of the Pacific-Antarctic Ridge during austral winter and spring (S. M. Hanchet et al., 2008). The Lagrangian particle tracking simulations suggest that the pathways and destination of juveniles depend on the exact spawning location and depth of transport (S. M. Hanchet et al., 2008). Their findings led to the hypothesis that eggs and juveniles entrained in the Ross Sea gyres are transported eastwards within the eastern Ross Gyre to settle out along the continental shelf and slope of the eastern Ross Sea and western Amundsen Sea. Alternatively, eggs may be transported westward to settle in the western Ross Sea, around the Balleny Islands and the adjacent Antarctic continental shelf. In the hypothesized life cycle, juvenile Antarctic toothfish move back towards the Ross Sea shelf as they grow, eventually moving into deeper water (S. M. Hanchet et al., 2008); after spawning, adults return to the continental slope in post-spawning migrations.

Empirical information on the timing of spawning or depth of transport are absent and plausible values were determined by finding spawning times and locations that resulted in successful transport to putative recruitment areas (S. M. Hanchet et al., 2008). The present study further develops the previous work by exploring the dependency of juvenile pathways and destination on the spawning location in more detail. In the present study, a series of Lagrangian particle

tracking simulations based on ocean and sea-ice velocities obtained from a high-resolution ocean model hindcast is used to determine the pathways of particles from five regions within the Ross Gyre under different advection schemes, which mimic different juvenile behaviours. The various advection schemes were designed to test the impact of ocean circulation, sea-ice drift as well as various biological strategies of toothfish (e.g. active swimming, diel vertical migration) on the trajectories and variability in success of particles in reaching the "target region".

The target region is defined as the stretch of ocean between the coast east of 155°W and 95°W and 100 km north of the 1000 m isobath, based on locations where the smallest demersal toothfish (~ 30 cm in length) have been observed (S. M. Hanchet et al., 2008).

2. Methods

a. Model setup

This Lagrangian dispersal study uses ocean and sea-ice data from a high-resolution ocean model hindcast. The ocean model is based on NEMO (Nucleus for European Modelling of the Ocean, Madec et al. (2017)) version 3.6 and uses LIM 2 (viscous-plastic) as a sea-ice model. A hindcast was generated for the period 1958-2019 using atmospheric boundary conditions from JRA-55-DO v1.3 (Tsujino et al., 2018). The oceanic model grid is based on a global eORCA1 configuration, which has also been used for New Zealand's Earth System Model (E. Behrens et al., 2020) and recent scientific studies to investigate marine heat waves in the Tasman Sea (Erik Behrens et al., 2019). An eddy-permitting (1/5°) grid spanning the southwest Pacific between 130°E to 86°W and 81°S to 25°S was embedded in the global non-eddy resolving model grid using the Adaptive Grid Refinement in Fortran (AGRIF, Debreu et al. (2008)) nesting capabilities of NEMO.

A second nest, with a resolution of 1/15°, was embedded in the southwest Pacific nest. This nest, hereafter called ROAM15 ('Ross Amundsen Sea 1/15 degrees'), spans the Ross and Amundsen Sea between 143°E to 95°W and 80°S to 57°S (Figure 1e). The nests and global model are coupled via a two-way nesting scheme and share the same vertical model grid with 75 vertical z-levels. The top level is 1 m thick, while the thickness increases to around 200m below depths of 4000 m. A partial cell parameterisation (Barnier et al., 2006) was applied to improve the representation of the bottom topography and overflows. The timestep for the global model is 30 minutes but is reduced to 10 minutes and 5 minutes for the southwest Pacific and ROAM15 nests, respectively. Viscosity varies between $1x10^4$ m^2/s (Laplacian), 5×10^{10} m^2/s (bi-Laplacian) and 1×10^9 m^2/s (bi-Laplacian) for the global eORCA1, and the southwest Pacific and ROAM15 nests, respectively. Diffusivity was set to 1000 m^2/s, 200 m^2/s, and 66 m^2/s accordingly.

The hindcast was started from rest with climatological values for temperature and salinity based on EN4 (Good et al., 2013) fields generated over the period 1995-2014. Ice-shelf cavities were not explicitly simulated but meltwater fluxes are prescribed at the front of the ice-shelf edge. Due to the incompatibility of the Lagrangian iceberg scheme with AGRIF, meltwater fluxes from icebergs were prescribed, based on a climatology of a hindcast without AGRIF nests.

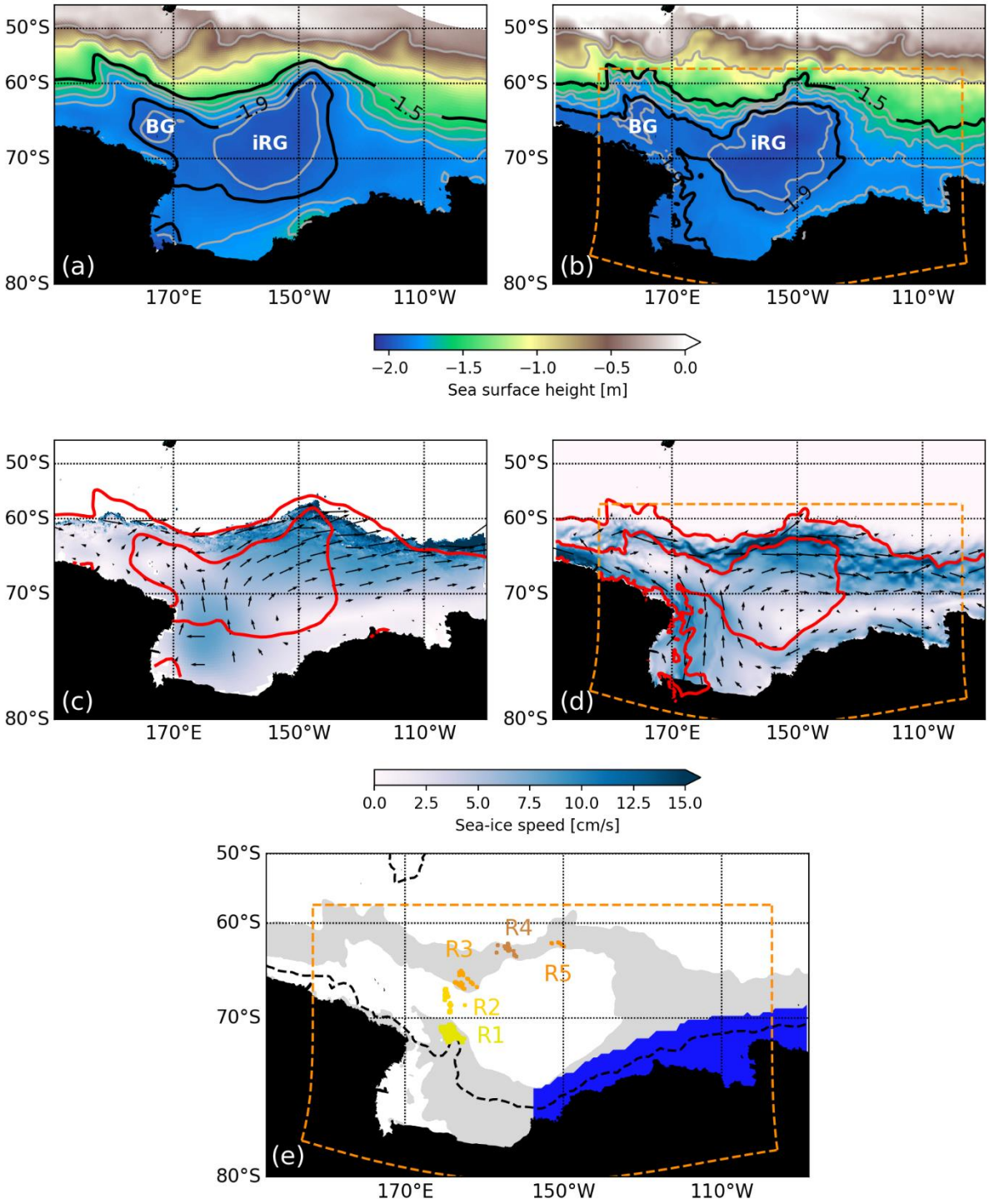

Figure 1: Mean (2011-2016) sea surface height from (a) Cryosat and (b) ROAM15 in colour and grey contours (interval is 0.1 m). The -1.9 and -1.5 m contour lines have been highlighted in black for a better comparison between observations and model results. The dashed orange line in (b), (d) and (e) illustrates the boundaries of the high-resolution nest (1/15°) within the 1/5° nest which covers the southwest Pacific. Mean June-September (2010-2017) sea-ice motion shown by the colour shading from (c) Pathfinder satellite product and (d) ROAM15 in cm/s. Every 10th or 30th velocity vector is drawn for Pathfinder and ROAM15, respectively. The red contour lines show the highlighted sea-surface height contours from (a) and (b) to illustrate the Ross Gyre boundaries. Two inner gyres, the Balleny Gyre (BG) and the inner Ross Gyre (iRG), are

contained within the Ross Gyre. (e) Particles were seeded in five clusters (R1-R5) located in the eastern and northern boundary of the Ross Gyre illustrated by modelled (2011-2016) sea surface height (grey area) between -1.9 m and -1.5 m. The 1000-m isobath of the continental shelf is shown by the black dashed contour line and the target region is indicated by the blue shaded polygon.

b. Model evaluation

Due to the dominance of sea-ice in the Ross and Amundsen Seas, winter observations are sparse or come with caveats reducing the ability to use them for model validation. However, progress has been made to produce satellite derived datasets allowing insights into the ocean dynamics of this region. Sea surface height characterises the near-surface ocean circulation and therefore can be used to visualise the Ross Sea gyre circulation (Armitage et al., 2018; Erik Behrens et al., 2016; Kwok & Morison, 2015; Meijers, 2014). Here we used the CryoSat-2 based product provided by Ron Kwok (https://swot.jpl.nasa.gov/documents/1541/?list=projects) which detects sea surface height in leads in the sea-ice pack and covers the period 2011-2016 (Kwok & Morison, 2015). In addition to the satellite product for sea-surface height, sea-ice velocities from the Pathfinder mission (https://nsidc.org/data/NSIDC-0116) were used for model validation.

The upper-ocean circulation of the Ross Sea is dominated by the Antarctic Slope Current and the cyclonic Ross Sea Gyre which is bounded in the north by the Antarctic Circumpolar Current. The Ross Sea Gyre is characterised by lower sea-surface height values (<-1.9m) and clearly visible in the CryoSat-2 sea-surface height product (Figure 1a). It comprises two inner gyres, an inner “Balleny Gyre” in the north-western part, and an “inner Ross Gyre”, which occupies the eastern part. In the remainder of the manuscript, we use the term Ross Gyre to describe the overall Ross Gyre circulation, which includes both inner gyres.

The modelled sea surface height pattern shows similar patterns to the observations (Figure 1b). In general, the boundary of the modelled Ross Gyre agrees well with the observations but expands too far south in the western Ross Sea and along the Oates Land coast, whereas observed Ross Gyre boundary only touches the Antarctic Coast near Cape Adare. Factors which potentially contribute to this discrepancy are the different horizontal resolutions of the satellite product (~25 km) and the model (<3 km) as well as the exact unknown reference level. In addition, the modelled Ross Gyre does not extend far enough into the Southern Ocean at the north eastern boundary as suggested by the observations. Despite the horizontal resolution differences, the model simulates both inner gyres and, in general, agrees well with the observed sea surface contours.

The satellite derived wintertime (June-September) sea-ice motion shows the northward drift over the western Ross Sea (Figure 1c). East of 150°W and north of around 70°S sea-ice is deflected to the east due to the prevailing westerly winds. In this area, the sea-ice motion is perpendicular to the Ross Gyre boundaries (illustrated by the -1.9 m sea-surface height contour) and causes sea-ice to be carried across the Ross Gyre boundary. The model results show the same

characteristics but with more detailed structure due to the finer model grid (~3 km; Figure 1d) compared to the satellite product (25 km). In the northeastern Ross Sea, the modelled sea-ice motion is more zonally directed than the observations, which means modelled sea-ice is not being carried as far north as the observations suggest. In addition, the model shows stronger sea-ice flow along the coast and within the energetic Antarctic Slope Current, which is not present in the satellite derived sea-ice drift. Reasons for the larger sea-ice flows in this region could be a case of a too strong coupling between ocean momentum and sea-ice drift in the model. Overall, the model appears to effectively capture the large-scale sea-ice drift.

c. Particle release strategy and tracking

Particles were seeded over 5 distinct regions within the Ross Gyre where mature female toothfish are prevalent (R1-R5, Figure 1e, S. Hanchet et al. (2015)). These regions are associated with seamounts in the northern Ross Sea and the shelf region around the Iselin Bank area. These regions are within the sea level range that connects the northern rim of the Ross Gyre with the shelf of Antarctica (grey shaded area). The southern spawning regions R1 and R2 are areas with high toothfish abundance and where adolescent and adult fish are observed (S. Hanchet et al., 2015).

Parcels (Delandmeter & van Sebille, 2019), an open-source Python based API for Lagrangian ocean analysis, was used to simulate the transport of virtual toothfish eggs and juveniles using environmental variables (ocean current velocities and sea-ice motion) from ROAM15. *Parcels* was chosen over other Lagrangian tracking tools such as *Ariane* (Blanke & Raynaud, 1997), *TRACMASS* (Döös et al., 2017) and *OpenDrift* (Dagestad et al., 2018) as it allows for flexible and modular particle advection and supports the NEMO ocean grids.

Every day between the 15th July through to 15th September - the assumed spawning season of toothfish (S. J. Parker et al., 2019) - 411 particles spanning the five spawning regions were released and advected for up to three years using the ocean and sea-ice fields from ROAM15. The number of particles released at each seeding location were scaled according to the size of the seeding location. This seeding procedure, with a total of 25,893 particles for each year, was repeated for every year from 2002 to 2016. The particle seeding was stopped in 2016 to allow for a 3-year particle advection. If particles reached the model domain boundary during that timeframe the tracking was stopped. Particles were advected using 5-daily averaged ocean and sea-ice fields from ROAM15 and the locations and velocities of each particle were archived as daily snapshots.

d. Particle advection schemes

The general particle advection is based on a Runge-Kutta 4th order advection with a timestep of 1 hour. Five variations to this general advection scheme were implemented to test the sensitivity of dispersal to assumptions about sea-ice advection (SA), ocean advection (OA), advection at depth (AAD), diurnal vertical movement (DVM) and active southward movement/velocity (SV) towards the Antarctic shelf (Figure 2).

Virtual eggs hatched after 100 days. After hatching variations in the particle behaviour were applied, while before hatching eggs were treated as passive particles drifting with ocean currents or sea-ice if it is present (Figure 2a).

Particles were seeded 50 m above the seamount, which were typically at depths of 1300 m, and floated to the surface with an average vertical velocity of 0.311 cm/s consistent with recent measurements of egg buoyancy (Parker et al., submitted). During the ascent through the water column particles were advected with the ocean currents. After 3.5–7.5 days the particles reach the surface. If the particles then encounter sea-ice they move with the sea-ice, otherwise they are advected with the ocean velocity in the surface layer (Figure 2a), which is 1 m thick in ROAM15. After 100 days, when the toothfish start their motile phase (Parker et al., submitted), they follow one of eight advection schemes (some with additional variations) for the remaining 944 days.

The eight advection schemes are graphically illustrated in Figure 2 and summarised in Table 1 along with the variations applied to some of the advection schemes. Below follows a brief description of the eight advection schemes:

1) Particles subjected to the sea-ice advection (SA) scheme (Figure 2b) were transported with sea-ice if it was encountered, otherwise they drifted with the ocean surface velocity;

2) The sea-ice advection or advection at depth (SA + AAD) scheme (Figure 2c) follows (1) but if no sea-ice was present the juveniles moved to a prescribed depth for shelter instead of staying at the surface and ocean velocity at this depth were used for the particle advection. We used depths of 200m or 400m here to test for the depth dependency of ocean currents;

3) The sea-ice advection or advection at depth and 12-hour DVM (diurnal vertical movement) (SA + AAD + DVM) scheme (Figure 2d) is similar to (2) but instead of staying at a fixed depth the juveniles performed a DVM between the specific depth and the surface and therefore encountered different ocean velocities as they moved through the water column. Similar to (2), a maximum depth of 200m or 400m was used;

4) The sea-ice advection with active southward swimming (SA + SV) scheme (Figure 2e) is similar to the advection scheme in (1) but an additional southward motion of either 500 m/day or 1000 m/day (based on assumed sustained swimming capabilities of juvenile toothfish) was applied after hatching to the particle velocities to simulate active swimming towards the Antarctic coast;

5) In the ocean advection (OA) scheme (Figure 2f) the presence of sea-ice was ignored, and the particles were advected with the surface ocean velocities regardless of whether sea-ice was present or not;

6) The ocean advection (OA) at depth (OA + AAD) scheme (Figure 2g) is the same as (5), however particles were advected at a prescribed depth of 200m or 400m;

7) The ocean advection at depth and DVM (OA + AAD + DVM) scheme (Figure 2h) is similar to (6) but instead of staying at a fixed depth the juveniles performed a 12-hour DVM between either 200m or 400m;

8) The ocean advection at the surface with active southward swimming (OA + SV) (Figure 2i) scheme is similar to (5) but an additional southward motion of 500 m/day

or 1000 m/day was applied to the particle velocities to simulate active swimming towards the Antarctic coast;

An additional scheme was designed where the particle advection changes from sea-ice advection (SA) to surface ocean advection (OA) after 180 days. This advection scheme tests the combined benefits of both schemes and explores the sensitivity of particle trajectories to changes in behaviour as they grow. For more details see section 3e.

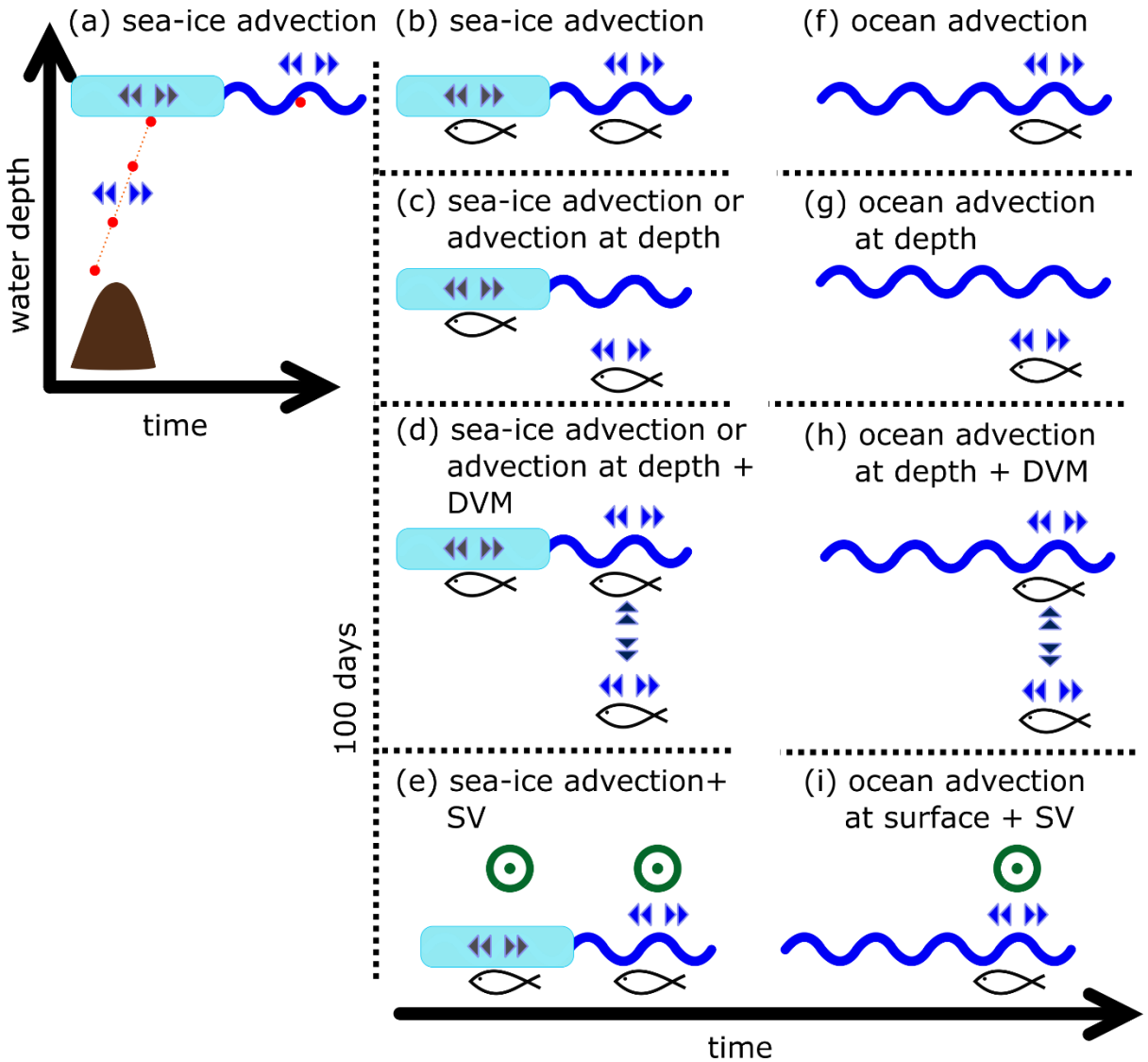

Figure 2: Advection schemes for the Lagrangian particle tracking: Every particle (red dots) is seeded 50 m above the sea floor at sites R1–R5. (a) Particles ascend to the surface with a vertical velocity of 0.311 cm/s and are advected with ocean motion until they reach the surface. If sea-ice is present (blue rectangle), sea-ice motion is used for particle advection otherwise surface ocean motion (blue wave) is used for 100 days. After hatching (100 days) the juveniles (fish symbols) are advected with one of the following advection schemes. (b) Sea-ice advection: if sea-ice is present sea-ice motion is used otherwise surface ocean motion; (c) Sea-ice advection or advection at a specific depth: same as (b) but particles drift at a specific depth (200 or 400m) if sea-ice is not present; (d) Sea-ice advection or advection at a specific

depth with diurnal cycle to the surface: same as (c) but juveniles perform a diurnal cycle between a specific depth and the surface if sea-ice is absent; (e) same as (b) but an additional southward velocity (SV) is applied to simulate active swimming of the juveniles towards Antarctica. (f) – (i) follows the sea-ice advection schemes (b) – (e) but ignores any sea-ice motion and uses ocean motion only for particle advection.

Table 1: Overview of all simulations. The letters correspond to the advection schemes illustrated in Figure 2.

	Within 100 days (pre-hatching)	After 100 days (post-hatching)
Sea-ice advection (SA)	(a) Sea-ice advection	(b) Sea-ice advection
Sea-ice advection or advection at depth (200m)	(a) Sea-ice advection	(c) Sea-ice advection or advection at depth
Sea-ice advection or advection at depth (400m)	(a) Sea-ice advection	(c) Sea-ice advection or advection at depth
Sea-ice advection or advection at depth (200m) + DVM	(a) Sea-ice advection	(d) Sea-ice advection or advection at depth + DVM
Sea-ice advection or advection at depth (400m) + DVM	(a) Sea-ice advection	(d) Sea-ice advection or advection at depth + DVM
Sea-ice advection + SV (500m per day)	(a) Sea-ice advection	(e) Sea-ice advection + SV (e)
Sea-ice advection + SV (1km per day)	(a) Sea-ice advection	(e) Sea-ice advection + SV
Sea-ice advection 180 days	(a) Sea-ice advection	(b) Sea-ice advection / (f) Ocean advection
Ocean advection (OA)	(b) Sea-ice advection	(c) Ocean advection
Ocean advection depth (200m)	(a) Sea-ice advection	(d) Ocean advection at depth
Ocean advection at depth (400m)	(a) Sea-ice advection	(g) Ocean advection at depth
Ocean advection at depth (200m) + DVM	(a) Sea-ice advection	(h) Ocean advection at depth + DVM
Ocean advection at depth (400m) + DVM	(a) Sea-ice advection	(h) Ocean advection at depth + DVM
Ocean advection (surface) + SV (500m per day)	(a) Sea-ice advection	(i) Ocean advection + SV
Ocean advection (surface) + SV (1000m per day)	(a) Sea-ice advection	(i) Ocean advection + SV

e. Particle separation, diagnostics and target region

For analysis, particles were separated into successful and unsuccessful particles. Successful particles were defined as particles which entered the target region within

three years of being released. However, particles did not have to remain in the target region to be classified as successful. Particles which never entered the target region were identified as unsuccessful.

To illustrate the dispersal of all released particles a 2-dimensional (longitude and latitude) cumulative probability function was calculated (Figure 4-5). The cumulative probability density function is the cumulative number of all particles (daily locations) over time in a 0.5°×0.5° grid box.

The same diagnostic was applied to illustrate the overall particle age (Figure 6). The individual particle locations in time were used to identify the corresponding 0.5°×0.5° grid box and the age of particles at that time was used to compute a time-average age for all particles in this grid box.

The arrival age for successful particles was computed (Figure 6 and 7). Here the particle age of its first entry into the target region was recorded and subsequent ages truncated.

3. Results

a. Success rate, travel times and seeding location dependency

The time-averaged success rates and travel time of successful particles over all seeding regions (R1-R5) are shown in Figure 3a, b. There is a clear distinction in the success rates of particles which use sea-ice motion versus particles which ignore its presence (Figure 3a). Particles that use sea-ice as a shelter and drift with it, without any active southward swimming, have a relatively low success rate (<8%, grey bars) in reaching the Antarctic continental shelf within a period of three years. Analogous ocean advected particles, on the other hand, show success rates of 12-24% (dark blue bars) suggesting a doubling to tripling of the relative success rate. Standard deviations for the sea-ice advected particles are in the same order of magnitude as the time-average. This suggests that the success is intermittent among years (primarily between 2006-2014, not shown), which explains the overall low success rates.

Sea-ice advection combined with either advection at a fixed depth or diurnal vertical movement under ice free conditions has no obvious impact on the success rate and shows similar success rates to the sea-ice advection schemes where particles stay at the surface. In contrast, simulations where an active swimming towards the Antarctic coast is incorporated show a significant increase in success rates. The mean success rate in these active swimming schemes increases from ~8% to around 25% with a swimming speed of 500 m/day and to nearly 50% if juveniles were to maintain a speed of 1000 m/day after hatching. While the standard deviation increases in these simulations the trend towards higher success rates with increased southward swimming appears to be robust, with success rates barely dropping below 15% for an individual release year (not shown).

In the ocean advection schemes, the spawning success is not intermittent between years, but the standard deviations are similar to the sea-ice advection schemes. Ocean advection combined with advection at a fixed depth results in a slight decrease in

success rates (~18% and 12% for advection at 200m and 400m, respectively) compared to the success rate of the ocean surface advection scheme (24%). The addition of diurnal vertical movement has no significant impact on the success rate and both simulations show success rates between 24% and 21% similar to the success rate of the ocean surface advection scheme. Comparable with the sea-ice advection schemes, the ocean advection schemes with active swimming towards the Antarctic coast have significantly higher success rates compared to the other ocean advection schemes. A swim rate of 500 m/day and 1000 m/day increases the success rate to more than 30%. However, the success rate does not increase with increased swimming rates (the relationship is non-linear).

In addition, the scenario where particles were subjected to sea-ice advection for the first 180 days followed by ocean advection for the remaining period (cyan bar) shows a success rate slightly higher (29%) than the success rate of the ocean surface advection scheme (24%). This suggests that the drift over the first 180 days might not be as important for the overall success rate, but more details are provided in section 3e.

The time-averaged travel times for all successful particles from all seeding locations are shown in Figure 3b. As with the success rate there is a clear contrast in the travel times of particles that drift with sea-ice and those that do not. Although the success rates for sea-ice advected particles are relatively lower, they reach the Antarctic shelf 100-200 days earlier than the purely ocean advected particles. The shorter travel times of particles subjected to the sea-ice advection schemes apply regardless of the particle release location (Figure 3d).

The time-averaged travel time for the sea-ice advected particles is around 650 days with a standard deviation of around 100 days (Figure 3b). There is no clear travel time dependency between the different sea-ice advection schemes, even for the schemes with active swimming that have higher success rates. The travel times for the ocean advection schemes vary between 650 and 850 days. Due to the larger number of successful particles the standard deviations are reduced (<100 days) compared to the sea-ice advection schemes. Particles subjected to ocean advection at a fixed depth or performing a diurnal vertical migration take longer (>800 days) to reach the Antarctic shelf compared to all other advection schemes. The addition of active swimming towards the Antarctic coast shortens the travel time by around 50 to 130 days, compared to the ocean surface advection scheme. This shorter travel time corresponds to increased success rates, as discussed above. The travel time of the simulation where sea-ice advection is applied for the first 180 days and ocean advection for the remaining period (cyan bar) shows a travel time very similar to the surface ocean advection schemes (see section 3e for more details).

The results above summarise the trajectories for particles released over all seeding locations (R1-R5). A more detailed breakdown of success rates and travel times for the five individual seeding regions is provided in Figure 3c-d. For the sea-ice advection schemes without active swimming, regions R3 and R5 show, in general, slightly higher (>5%) success rates compared to the other seeding regions. For sea-ice advection at a fixed depth higher success rates are also seen for R1. It appears that for these schemes the “distance to the target region” – measured in terms of clockwise circulation around the inner Ross Gyre – is not the prime factor controlling the success rate. For the sea-ice

advection schemes with active swimming, the success rates increase for all seeding regions, although not uniformly. The increase in success rates for R1 (by 200% and 700%) and R2 (by 150% and 750%) is higher than for R3 (by 50% and 325%), R4 (by 50% and 400%) and R5 (by 30% and 360%) for swimming speeds of 500m/day and 1000 m/day, respectively.

The ocean advection schemes show higher success rates (>15%) for R2, R3 and R5, compared to R1 and R4. Similar to the sea-ice advection schemes, the ocean advection schemes with active swimming show a non-uniform increase in success rates. The increase in success rates for R4 (233%, 350%) and R5 (133%, 233%) are higher than for R1 (100%, 100%), R2 (100%, 75%) and R3 (100%, 100%) for swimming speeds of 500m/day and 1000m/day, respectively. For the sea-ice advection schemes the regions R1 and R2, furthest in distance from the target region, show the biggest increase in success rate while for the ocean advection schemes the regions closer to the target region (R4 and R5) show a larger increase.

For the individual seeding locations (Figure 3d), a coherent increase in travel times with increasing distance from the target region is visible for all scenarios (R1>R2>R3>R4>R5). The travel times are relatively insensitive to the choice of the sea-ice advection scheme. As seen in Figure 3b, the travel times of the ocean advection schemes are more variable than that of the sea-ice advection schemes. This is also evident for the individual seeding locations, which show a larger spread between the ocean advection schemes. In the schemes where active swimming is applied the travel time reduces for all seeding locations, except for R4 and R5.

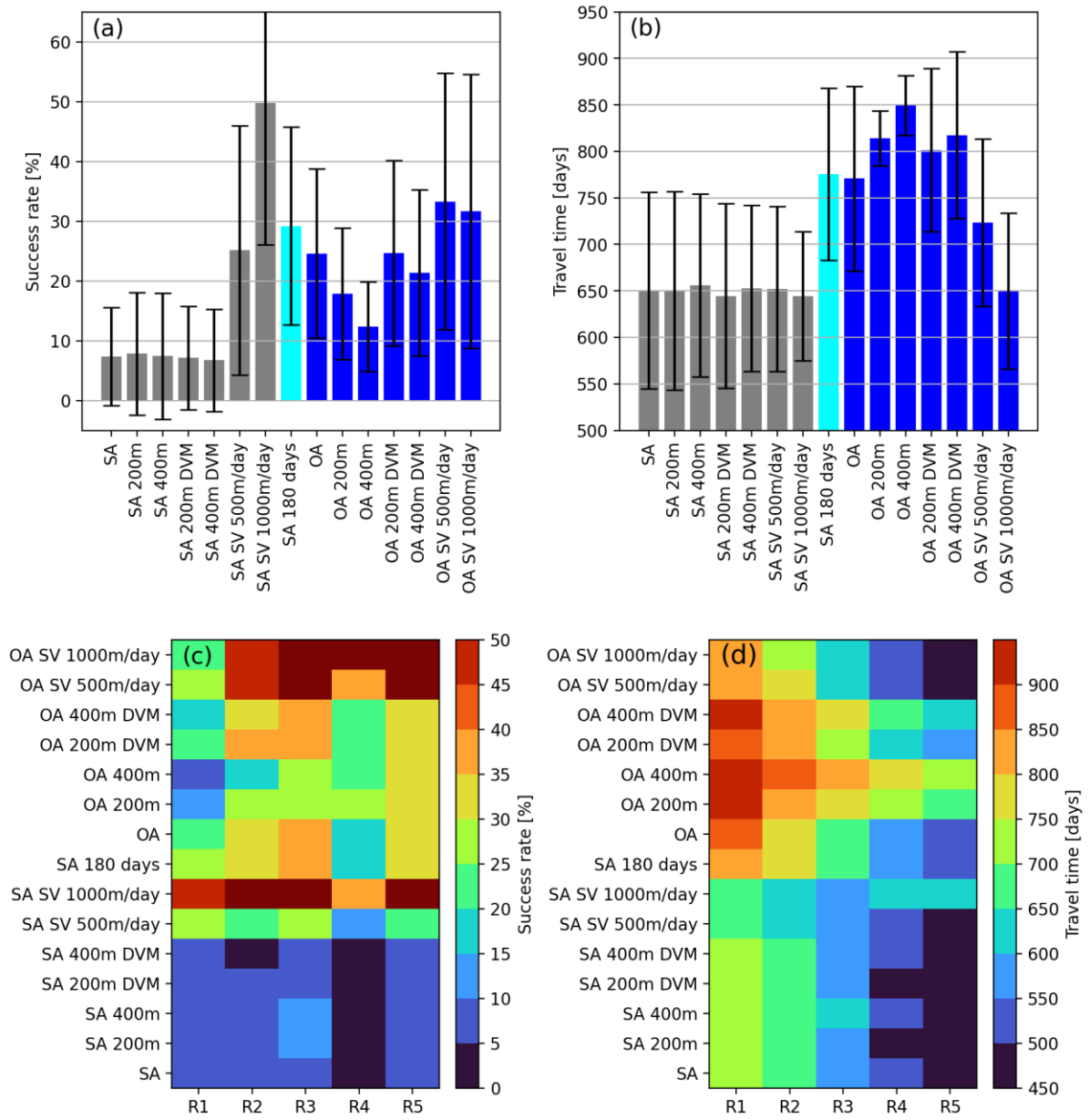

Figure 3. (a) Time-averaged success rates: Fraction of particles seeded in regions R1 to R5 that made their way into the target region (blue shaded region in Figure 1e) within three years. SA refers to sea-ice advected particles, while OA refers to ocean advected particles, SV to southward velocity and DVM to diurnal vertical movement. (b) Time-mean travel times in days for successful particles. The grey bars show results for experiments which are based on SA while the blue bars are based on OA. (c and d) Time-mean success rates and travel times of successful particles from the various advection schemes in relation to the seeding locations (R1 to R5).

b. Cumulative Probability density function and mean pathways

The daily recorded particle positions (2002-2018) for selected advection schemes were used to compute a cumulative probability density function. The cumulative probability density function and average particle trajectories were computed for unsuccessful (Figure 4) and successful (Figure 5) particles separately. The probability density function is only presented for a subset of scenarios, since the differences between the individual scenarios are minor.

The vast majority of particles subjected to the sea-ice advection scheme that fail to reach the target region are zonally transported out of the Ross Sea region at a latitude of around 65°S (Figure 4a). A considerable number of particles, however, recirculate in the Ross Sea and Ross Gyre but are not advected south enough to enter the target region. The mean pathways for seeding regions R1, R2, R3 and R5 are very similar, but the timing when particles reach a certain point differ for each release region. Only the mean pathway for seeding region R4 shows a slightly more northward shifted pathway compared to the others. The cumulative probability distribution and pathways for the sea-ice advection scheme with a fixed depth of 200m (Figure 4c) is qualitatively very similar to the pattern of Figure 4a, corresponding with similar success rates and travel times for both schemes.

Under the sea-ice advection scheme with additional active southward swimming, more particles are recirculated within the Ross Sea and Ross Gyre (Figure 4e) compared to the other two sea-ice advection schemes (Figure 4a and c). In addition, the inclusion of active swimming also tends to shift the mean trajectories of the unsuccessful particles slightly southward. This southward shift in the mean trajectories is more pronounced east of ~140°W. The considerable similarity between the three sea-ice advection schemes indicates that the trajectories of the unsuccessful particles are largely determined by the sea-ice motion and surface ocean circulation rather than circulation at depth or behaviour. However, the southward shifted trajectories in the active swimming schemes increases the likelihood that particles reach the target region.

Unsuccessful particles from the ocean advection scheme with no additional behaviour show a similar pattern to the sea-ice advection schemes, however the fraction of particles that recirculates into the Ross Sea without reaching the target region is larger (Figure 4b). This is also visible in the slightly southward shifted mean pathways for the five seeding locations.

The particles that fail to reach the target region under the ocean advection scheme that includes advection at a fixed depth show markedly different trajectories. Most of the unsuccessful particles, mainly from release zones R1-R3, are entrained within the Ross Gyre and thus do not leave the Ross Sea (Figure 4d). Even though these particles remain in the Ross Sea, they are not transported far enough south within three years to reach the target region. Particles released from R4 and R5, on the other hand, display trajectories similar to the sea-ice advection schemes and leave the domain at around 65°S. Similar to the ocean advection at depth scheme, the majority of unsuccessful particles from the ocean advection scheme with active swimming towards the Antarctic coast are recirculated within the Ross Sea via the Ross Gyre (Figure 4f). However, the

southward extension is more contracted compared to the advection at depth scheme. As with the corresponding sea-ice advection scheme, the mean particle trajectories are shifted slightly southward.

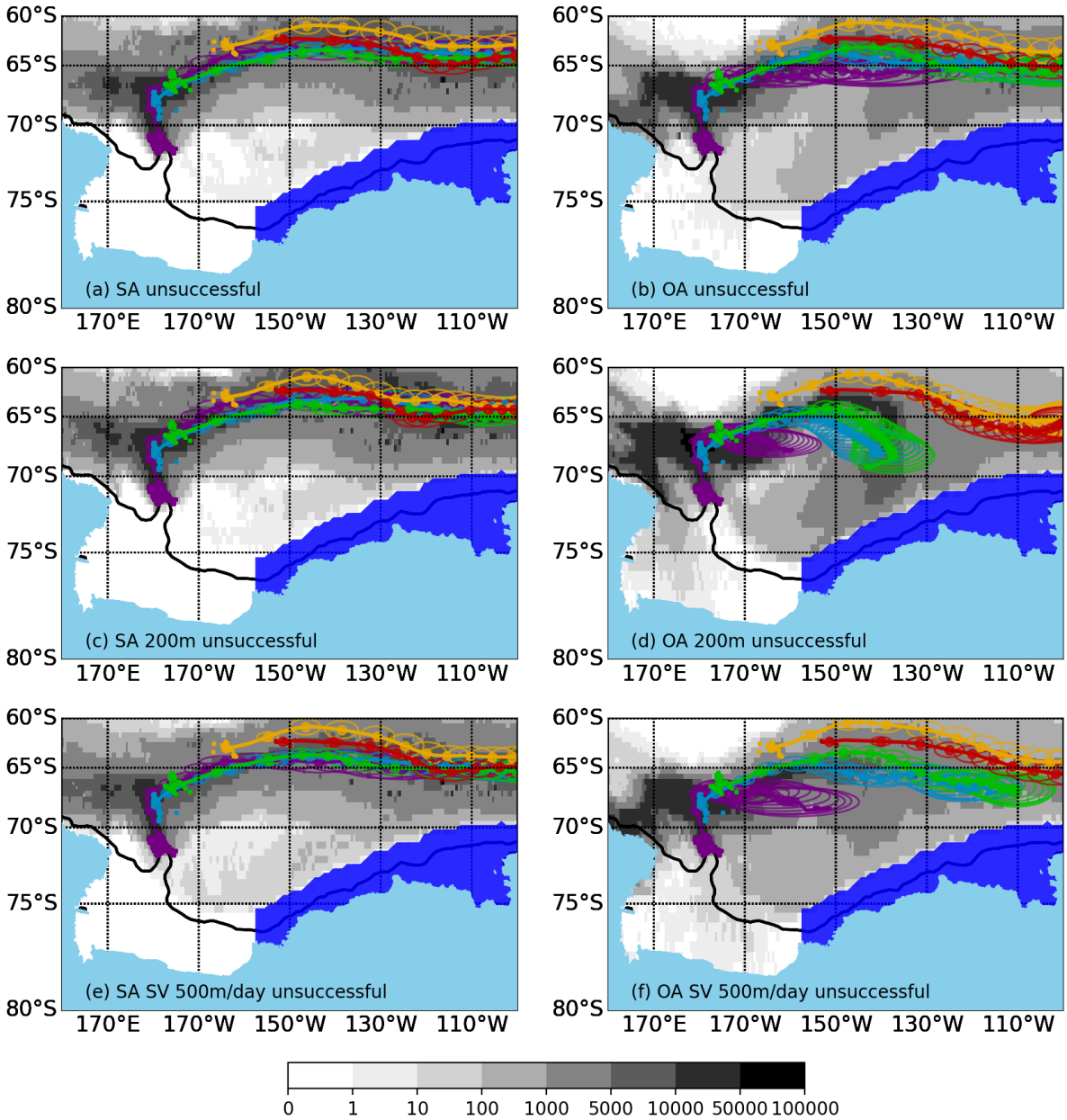

Figure 4. Cumulative probability density function (gray pixels, release years 2002-2016) for unsuccessful particles from different advection schemes. Unsuccessful particles are defined as particles that fail to reach the target region (dark blue polygon) in three years. Note the non-linear scale. Solid lines represent the mean trajectories of the unsuccessful particles released from R1 (purple), R2 (light blue), R3 (green), R4 (orange) and R5 (red). The dots and ellipses along the trajectories are 50 days apart. Coloured ellipses illustrate the particle spread, calculated by the standard deviation from all particle locations at that point in time. (a) Sea-ice advection (SA); (b) Ocean advection (OA); (c) Sea-ice advection or ocean advection at depth (200m); (d) Ocean advection at depth (200m); (e) Sea-ice advection + SV (500m/day); (f) Ocean advection + SV 500m/day. The black contour line marks the 1000m isobath.

Successful particles from the selected sea-ice advection schemes all follow approximately the same trajectory (Figure 5a, c, e). Over the first 100 days, the successful trajectories are very similar to the trajectories of the unsuccessful particles; however, the successful particles are then deflected southward between 140-130°W and do not continue along the zonal path. After their southward deflection, the majority of particles then veer to the east and enter the target region between 120-100°W. Only a few particles enter the target region west of 120°W. The southward deflection of successful particles tends to occur further west (~140°W) for particles released from R1, whereas particles released from R4 and R5 change direction further to the east (~130°W). Particles released at the southernmost release locations (R1 and R2) tend to follow a more direct route across the Ross Sea towards the target region.

The distribution of successful particles from the selected ocean advection schemes shows more confined pathways to the target region (Figure 5b, d, f) compared to their sea-ice advection counterparts. They also tend to enter the target region further to the west (130-110°W). This is particularly evident in the advection at depth scheme (Figure 5d). The trajectories of successful particles from the ocean advection schemes seeded from R4 and R5 are, in general, similar to those from the sea-ice advection schemes. However, after turning southward between 140-130°W, the successful particles from the ocean advection schemes continue to the target region along a more southward trajectory compared to the more easterly pathway of the sea-ice advection schemes. The trajectories from R1 to R3 reach around 3° further north compared to the sea-ice advected particles. North of the target region, particles from the ocean advection scheme that includes advection at depth are deflected to the west within the Antarctic Slope Current (Figure 5d). The mean trajectories of the ocean advection scheme with no additional behaviour (Figure 5b) and the scheme with active southward swimming (Figure 5f) suggests that the entry of successful particles into the target region occurs in two clusters, an eastern and western cluster. Particles from R4 and R5 enter the target region at the cluster centered on 120°W, while particles from R1, R2, and R3 tend to enter the target region at the cluster further to the west (centered on ~125°W and ~130°W for the scheme with no additional behaviour and the scheme with active swimming, respectively).

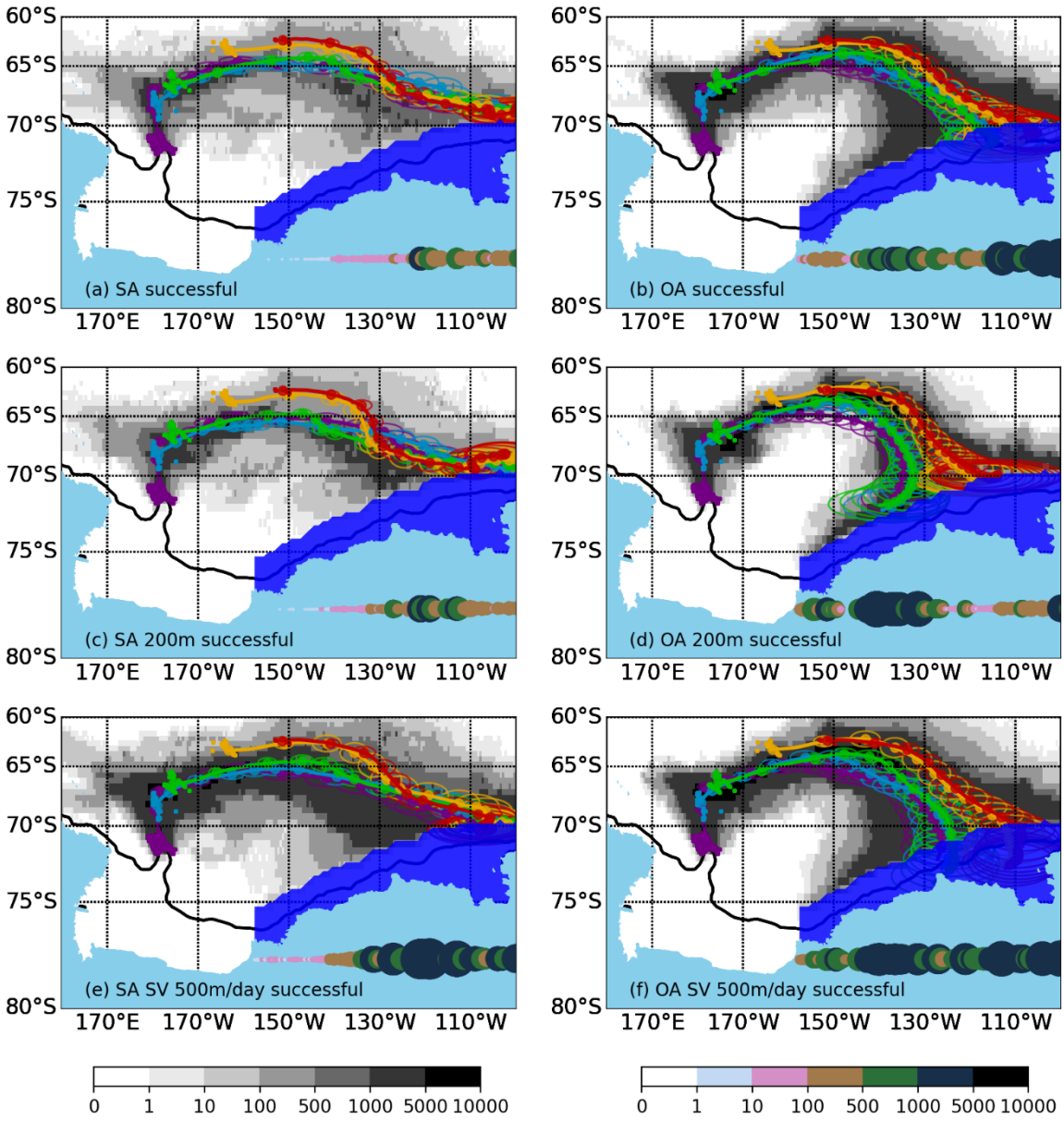

Figure 5. The same as Figure 5 but for successful particles. Successful particles are defined as particles that reach the target region (dark blue polygon) within three years of their release. Note the non-linear scale. Solid lines represent the mean trajectories of the successful particles released from R1 (purple), R2 (light blue), R3 (green), R4 (orange) and R5 (red). The dots and ellipses along the trajectories are 50 days apart. Coloured ellipses illustrate the particle spread, calculated by the standard deviation from all particle locations at that point in time. The color-coded and differently sized markers on the bottom right of each panel shows the distribution where (longitudinally) the particles have entered the target region and the number of particles at this location. (a) Sea-ice advection (SA); (b) Ocean advection (OA); (c) Sea-ice advection or ocean advection at depth (200m); (d) Ocean advection at depth (200m); (e) Sea-ice advection + SV (500m/day); (f) Ocean advection + SV 500m/day. The black contour line marks the 1000m isobath.

c. Particle age distribution

The daily recorded particle positions and particle age (2002-2018) for selected advection schemes were used to compute the particle age distribution binned onto a 0.5°×0.5° grid (Figure 6), i.e., each grid cell depicts the sum of the average age of particles on each day over the three years. As expected, the age of particles increases as they are advected away from the seeding locations. The age of unsuccessful particles from the three selected sea-ice advection schemes increases mainly as a function of longitude (Figure 6 a,e,i), although relatively low particle ages are present in the central Ross Sea, due to fast recirculation within the gyre. East of 110°W and north of 67°S, unsuccessful particles from the sea-ice advection scheme with no additional behaviour and the advection scheme with additional active southward swimming are older than 600 days, while those from the sea-ice advection scheme with advection at depth are >100 days older. Particles advected into the Ross Sea but not into the target region have an age of around 150 days. However, particles from the sea-ice advection scheme with active swimming that are advected into the Ross Sea via the Antarctic Slope Current tend to be 100-200 days older compared to the other two sea-ice advection schemes.

The age of unsuccessful particles from the three selected ocean-advection schemes is predominantly a function of latitude (Figure 6 c,g,k) in contrast to the sea-ice advection schemes. The oldest particles (>800 days) occur south of 70°S in the Antarctic Slope Current and the Ross Sea. South of 65°S unsuccessful particles from the ocean advection scheme with a fixed depth and with active swimming tend to be ~100 days older compared to the ocean-advection scheme with no additional behaviour.

The age of successful particles from the three sea-ice and ocean advection schemes tend to increase zonally and meridionally (Figure 6 b,d,f,h,j,l). Particles from the three sea-ice advection schemes reach the target region with ages between 200 and 600 days, with older particles occurring east of 130°W (Figure 6 b,f,j).

Successful particles from the three ocean advection schemes (Figure 6 d,h,l) are ~200 days older upon reaching the target region compared to their sea-ice advection counterparts. In addition, particles from the ocean advection scheme with advection at depth are 50-100 days older when they reach the target region compared to particles from the ocean advection scheme with no additional behaviour. This reflects the slower ocean velocities at depth compared to those at the surface. Conversely, successful particles from the ocean advection scheme with active southward swimming are ~50 days younger when they reach the target area.

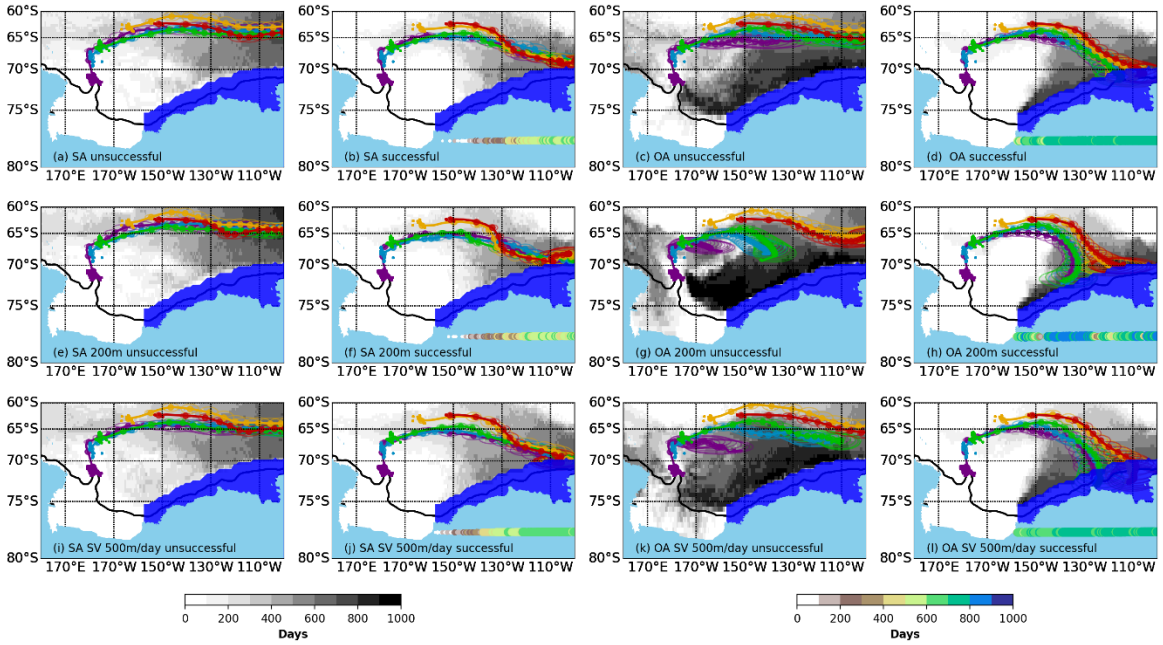

Figure 6. Time-averaged age distribution (release years 2002-2016) for different advection schemes and two sets of particles, unsuccessful and successful. Successful particles have reached the target region within 3 years after their release. The age distribution shows the time-averaged age (in days) since their release binned onto a 0.5°×0.5° grid. Solid lines represent the mean trajectories of particles released from R1 (purple), R2 (light blue), R3 (green), R4 (orange) and R5 (red). The dots and ellipses along the trajectories are 50 days apart. Coloured ellipses illustrate the particle spread, calculated by the standard deviation from all locations at that point in time. The color-coded and differently sized dots in the successful particle panels show the age versus longitude distribution when particles have entered the target region. (a-b) Sea-ice advection (SA); (c-d) Ocean advection (OA); (e-f) Sea-ice advection or ocean advection at depth (200m); (g-h) Ocean advection at depth (200m); (i-j) Sea-ice advection + SV (500m/day); (k-l) Ocean advection + SV 500m/day. The black contour line marks the 1000m isobath.

d. Age at arrival in the target region

In this section, the age at arrival and influx (number of particles per day) of successful particles into the target region is explored for each seeding location for selected advection schemes (Figure 8). The particle influx to target region for each release region was computed relative to the total number of successful particles over time (100%). For the sea-ice advection scheme (Figure 8a), the very first particles reach the target region about 260 days after release and originate from regions R4 and R5, which are the closest to the target region in terms of the clockwise Ross Gyre circulation. After 320 days particles from R3 start to enter the target region and particles from region R2 reach the target region ~380 days after release. At that point, the peak in the influx of particles is reached with 1.5% per day, where particles from R4 and R5 contribute the largest portion. Around day 440 the first particles from region R1 emerge in the target region. At the same time the contribution of particles from region R4 and R5 shows a sharp decline, leading to a minimum in the influx rate. This decline is compensated quickly by an increasing contribution from R2 and R1 until day 560, where the contributions from all regions show a drop at that point in time. Day 560 describes roughly the start of the

summer season of the second year. By then more than 50% of all successful particles have reached the target region. The influx of particles increases after that until day 680, where particles from region R1 contribute the majority. After day 680 the influx of particles starts to generally decline and the remaining 25% of particles reach the target region. Particles arriving at the target region after day 680 mainly originate from region R1, R2, and R3. However, there is a small influx of particles from R4 and R5 which suggests that particles have recirculated through the Ross Sea.

For the ocean advection scheme (Figure 7b), particles from seeding regions R1 to R5 start to appear at similar times as sea-ice advected particles. However, the influx rates of particles increase more gradually compared to the sea-ice advection scheme. By day 640 the maximum influx rate of around 1% per day is reached, that is when the contribution from region R1 is largest, while contribution from region R4 and R5 are already declining. At that point 50% of all successful particles have already reached the target region, which is roughly 100 days later than in the sea-ice advection scheme. The contribution from region R2 and R1 stays fairly constant until day 1000, while the total influx rate declines. Overall, the ocean-advection scheme shows a less variable but a prolonged influx of particles into the target region.

The distribution for sea-ice advected particles with advection at 200m under ice-free conditions (Figure 7c) is similar to the purely sea-ice advection scheme (Figure 7a). However, this scheme shows a stronger separation of particles into two temporal modes, with a distinct decline in particle fluxes around day 560 (the second summer season). As in the purely sea-ice advection scheme more than 50% of all particles have reached the target region by this time.

The timing of first arrival of particles in the ocean advection at 200m depth scheme (Figure 7d) is similar to the ocean advection at the surface (Figure 7b). However, the influx rates remain lower compared to the surface ocean advection scheme for the first 700 days but exceeds that for the remaining period. Due to the slower velocities at depth, the arrival of particles in the target region is delayed in comparison to advection at the surface. This is illustrated by the fact that 50% of all particles reach the target region ~750 days after release. Therefore, particles subjected to the ocean advection at depth scheme reach the target region around 100 days later compared to the surface ocean advected particles.

The distribution in sea-ice advection scheme with active swimming (Figure 7e) changes only slightly in comparison to the sea-ice advection without active swimming (Figure 7a). The active swimming reduces the travel time by about 20 days for most seeding locations and the peak centered on day 650 gets narrower with higher influx rates. About half (50%) of the particles released have reached the target within 520 days. A further peak emerges around 980 days, which represents particles that have looped around the inner Ross Gyre one more time and have reached the target region as a result of active swimming.

A slightly earlier arrival of particles is also visible in the ocean advection scheme with active swimming (Figure 7f) in comparison to the ocean advection scheme without active swimming, while the overall distribution is very similar. About half (50%) of the

particles released have reached the target region within 620 days. For the remaining period the influx rates are lower than for the ocean advection scheme without active swimming.

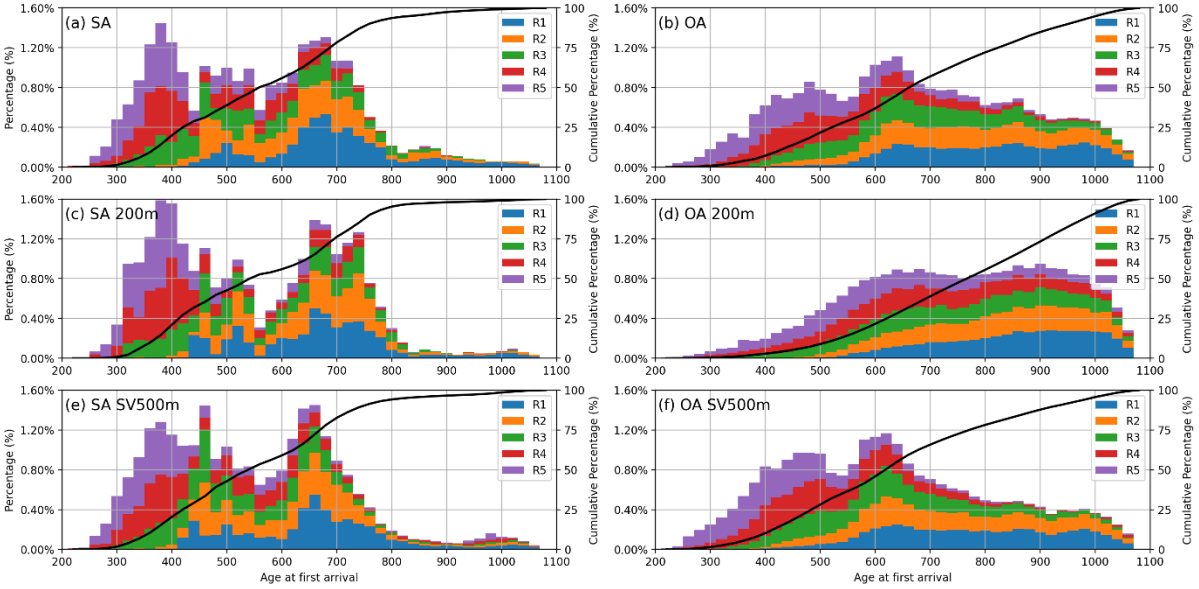

Figure 7: The age at fist arrival for successful particles from selected sea-ice and ocean advection schemes versus influx rate (%). The area under the color shaded area is 100%. (a) Sea-ice advection, (b) Ocean advection, (c) Sea-ice advection or advection at 200m, (d) ocean advection at 200m, (e) Sea-ice advection and active swimming of 500 m/day and (f) Ocean advection and active swimming of 500 m/day. Age bins are 20 days apart. The color-coding represents the contribution from the individual release regions. The black line shows the cumulative percentage of particles which have reached the target region.

e. The importance of the 2nd winter season to reach the target region

As juvenile Antarctic toothfish grow, their behavior might change to influence their transport success. An advection scheme was designed which switches from sea-ice advection to surface ocean advection after 180 days. This scheme combines the benefits of the sea-ice and ocean advection schemes and therefore, results in an increased success rate compared to the majority of other advection schemes (see section 3a). Day 180 marks the first summer season when most particles experience open ocean conditions and therefore the transition from sea-ice to ocean advection does not introduce an artificial adjustment. In early life stages, sea-ice appears beneficial since it provides shelter and food. Therefore, drifting with the sea-ice is likely to be beneficial. However, particles in the second winter are typically found at the northern boundary of the inner Ross Gyre depending on release location. Observations and model results show that sea-ice drift in this region is predominately to the east and north-east (Figure 1c, d), which would transport particles out of the inner Ross Gyre, towards the ACC and away from the target region.

Figure 8 shows the mean trajectory for the advection scheme that switched from sea-ice to ocean advection after 180 days (SA 180 days) in comparison to the trajectories from sea-ice and surface ocean advection schemes. These trajectories were generated by averaging all particle locations (successful and unsuccessful) over

a certain time period. Note that for the first 100 days the trajectories for all advection schemes are identical since they all follow the sea-ice advection scheme until the eggs hatch.

For the release region R1 the trajectories are shown in Figure 8a. After release, the particles travel north and turn north-eastward after about 60 days. By day 250 (red dots), the beginning of the second winter season, the trajectories of the different schemes divert substantially. However, before day 250 the trajectories for all schemes are barely spatially indistinguishable. In addition, particles from the surface ocean advection scheme travel slower compared to the other two schemes. For the sea-ice advection scheme (dark blue trajectory), the fast-eastward spreading is clearly visible after day 250, and juveniles are transported across the Ross Gyre boundaries illustrated by the sea-surface height contour lines (black, adopted from Figure 1). After two years the sea-ice advected particles have reached 115°W and 64°S. In comparison, the surface ocean advected particles (green) have reached 145°W and 66°S and are still within the Ross Gyre boundaries. The particles with the behavior change (light blue) have traveled slightly further east (137°W) with their trajectories pointing towards the target region.

For the other release regions, a similar behavior is observed, with sea-ice advected particles always further north and east and further away from the target region compared to the other two advection schemes (Figure 8b-e). Although the initial particle trajectory for release region R2 (Figure 8b) differs more, by day 250 the trajectories are in close proximity again, which puts the particles with the behavior change (light blue) onto a very similar trajectory as for surface ocean advection. After two years the particles in these two advection schemes are relatively close to the target region. A very similar behavior is visible for particles seeded in region R3 (Figure 8c). For region R4 and R5 the general behavior changes and trajectories for the surface ocean advection scheme and the scheme with behavior change start to drift away from the target region and align more with the trajectory of sea-ice advected particles. This is because both seeding locations are already very close to the gyre boundary compared to seeding locations R2-R3, which show overall larger success rates than R4-R5 (Figure 3c). Beside the reduction in success rates for R4 and R5 the notion that sea-ice advection during the second winter is not beneficial remains true since the sea-ice drift carries the particles far away from the target region in comparison to particles which are carried by ocean currents alone.

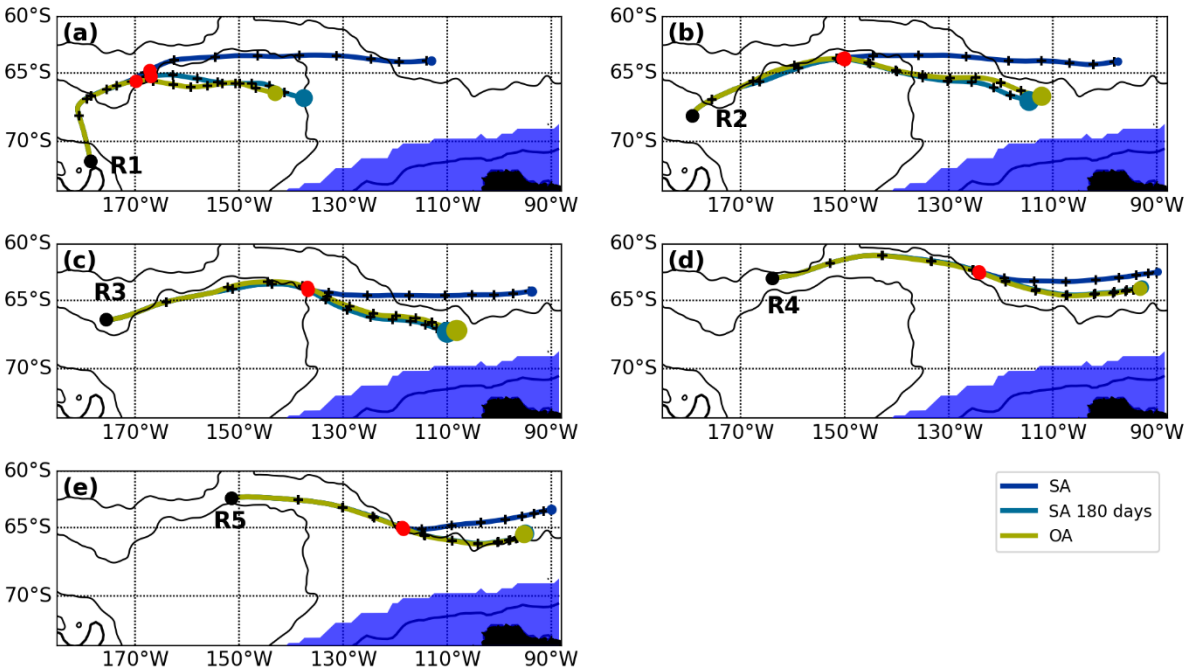

Figure 8. Mean trajectory for all released particles for seeding locations (a) R1, (b) R2, (c) R3, (d) R4, and (e) R5 for sea-ice advection (SA), sea-ice advection 180 day (SA 180 days) and ocean advection (OA) schemes over the first two years. The red dot marks the 250-day mark, approximately the start of the second winter season. The black + symbols on top of the trajectory are 60 days apart. The mean location of particles after two years is shown by a color-coded dot. The size of the dots at the end of the trajectory indicates the average success rate for the individual schemes.

4. Discussion and conclusion

The current knowledge about the early life history of Antarctic toothfish (*D. mawsoni*) life cycle is limited, and several key questions are still not fully understood: What is the spatial extent of spawning? How do eggs and juveniles manage to get from the spawning grounds to the shelf region? What role does sea-ice drift and ocean currents play?

This paper has investigated some scenarios around how potential spawning grounds could be connected to the shelf regions where the juvenile toothfish are found. The results from this study provide some insights about the spawning success for certain spawning regions and how that is influenced by sea-ice drift and ocean currents. In addition, the potential role of juvenile behaviour impacting the spawning success was investigated. While this paper covers a large set of scenarios it cannot explore all sensitivities and all possible scenarios. As our knowledge advances with time these scenarios will be revised, refined and potentially falsified.

In particular, we have not continued to track the juveniles into adulthood as there seem to remain unanswered questions concerning the timing of depth-dependent development of the toothfish in terms of being neutrally buoyant and/or being bottom dwelling (e.g. see the discussions and modelling in Ashford et al. (2017); and Ashford et al. (2012)). The relatively high horizontal and vertical resolution of the ROAM15 grid (but presently without tides and the Ross Ice Shelf) suggests that we could continue to track toothfish development onto and

then presumably off the Ross Sea continental shelf as they mature, potentially enabling a complete hypothetical life history using the model hydrodynamics and tracking. As before, future advances in understanding would make testing the juvenile to adult toothfish more tractable.

The particle tracking presented here uses hydrodynamic data from a high-resolution ocean model, ROAM15. This model captures the ocean circulation and sea-ice drift of the Ross Sea better than other ocean models, due to its fine model grid. The modelled oceanic circulation and sea-ice drift compares well to observations, which is key for Lagrangian studies. However, there are model biases in both ocean circulation and sea-ice drift which will impact the dispersal of particles. Some uncertainties also exist around the observational datasets since measuring sea-surface height during winter, when sea-ice is present, is difficult. The large number of released particles and a release period over 14 consecutive years reduces some of the model uncertainties and increases the confidence of the obtained model results, since averaging statistics could be applied.

A diagnostic which measures the success rate of particle arrival at the Ross Sea continental shelf regions was used to argue that some scenarios are more beneficial for recruitment to the toothfish population in the Ross Sea. However, even very small success rates, as estimated for particles advected with sea-ice drift, could be sufficient to sustain a population. Observed age-class distribution of Antarctic toothfish (not shown) suggest individuals present in each age class. This requires an influx of sufficient juveniles every year which the modelled sea-ice advection scenarios were unable to reproduce unless a strong southward active swimming (1000m / day after hatching) was incorporated. This suggests that juveniles transported purely with sea-ice drift require an additional behaviour change in order to reach the target region.

Observations and model results show a coherent pattern regarding sea-ice drift in the northern and eastern Ross Sea, where sea-ice drift is directed away from the target region. When juveniles pass through this region and follow the sea-ice drift they are likely carried away from the target region into the open ocean. It is therefore concluded - despite uncertainties around the modelling - that sea-ice drift in this region reduces the spawning success, with the modelling providing some solutions of how the juveniles could overcome this issue.

The modelling results show a sensitivity to the choice of the target region. A very general and inclusive approach has been used in this study to define a “target region” comprising the shelf region in the eastern Ross and Amundsen Sea based only on the locations of the smallest (and therefore youngest) toothfish observed in fishery data (S. Hanchet et al., 2015). The success rates and related pathways do change if the target region is modified; a target region located further north leads to generally higher success rates due to the recirculation of particles in the Ross Gyre; a more southern target region reduces the overall success rate accordingly. The change in the overall success rate is spread relative evenly over the different seeding regions. Restricting the region further to the east of 155° W leads to a reduction in the overall success rates, evenly spread over all seeding regions. Note the eastern extension of the target region is limited by the boundary of the nested model domain, which ends at 95°W.

The presented success rates are only based on dispersal by physical variables using particles with some simple assumed behaviours. Juveniles in the real ocean are affected by additional

factors, which have been neglected, but will impact the survival. One missing aspect is the food availability for the larvae and juveniles during their journey, which depends on various bio-physical properties (e.g. temperature, chlorophyll-a concentration, zooplankton abundance) and varies in space and time. This is one of the proposed benefits of sea-ice, as the productivity derived from melting sea-ice could provide a predictable and rich food source for juveniles. It is possible that the higher success rates with ocean advected particles could be impacted and reduced by lower food availability and longer exposure to open ocean predators. Reaching the target region early could be beneficial since the continental shelf could provide a rich food source and shelter. Also, the advection schemes with active swimming did not take into account the additional energy required in this process, which could lead to reduced success rates in reality. The advection schemes with DVM perform a repetitive 12-hour cycle between surface and a given depth, however these high latitudes experience a large seasonal cycle in daylight length. In which way this simplification affects the results is unknown and should be considered in future studies.

The results of this modelling study contrast with the expected distributions of juveniles which is based on observations of fish sizes to recruit to the continental slope of the Amundsen Sea. Observations of egg buoyancy indicate that eggs would be distributed at the surface, and therefore would be strongly associated with sea-ice. Therefore, the pattern of advection of juveniles under all scenarios except directional swimming, suggests that Antarctic toothfish must show a behaviour that modifies their trajectories once hatched. Observations of juvenile toothfish vertical distribution and swimming abilities especially after their first winter would greatly improve the ability to model the trajectories.

5. Acknowledgements

This project obtained funding from Ministry for Business Innovation and Employment via C01X1710 Ross Ramp and C01X1902 Deep South National Science Challenge. We acknowledge the support of NeSI High Performance Computing Facility and its team. Finally, I would like to acknowledge my partner and son. Model and trajectory data can be freely obtained via https://doi.org/10.5281/zenodo.4570967 , https://doi.org/10.5281/zenodo.4574388 and https://doi.org/10.5281/zenodo.4574418 .

6. References

Armitage, T. W. K., Kwok, R., Thompson, A. F., & Cunningham, G. (2018). Dynamic Topography and Sea Level Anomalies of the Southern Ocean: Variability and Teleconnections. *Journal of Geophysical Research: Oceans, 123*(1), 613-630. https://agupubs.onlinelibrary.wiley.com/doi/abs/10.1002/2017JC013534

Ashford, J., Dinniman, M., & Brooks, C. (2017). Physical-biological interactions influencing large toothfish over the Ross Sea shelf. *Antarctic Science, 29*(6), 487.

Ashford, J., Dinniman, M., Brooks, C., Andrews, A. H., Hofmann, E., Cailliet, G., et al. (2012). Does large-scale ocean circulation structure life history connectivity in Antarctic toothfish (Dissostichus mawsoni)? *Canadian Journal of Fisheries and Aquatic Sciences, 69*(12), 1903-1919.

Barnier, B., Madec, G., Penduff, T., Molines, J. M., Treguier, A. M., Le Sommer, J., et al. (2006). Impact of partial steps and momentum advection schemes in a global ocean circulation model at eddy-permitting resolution. *Ocean Dynamics, 56*(5-6), 543-567. <Go to ISI>://WOS:000243189900014

Behrens, E., Fernandez, D., & Sutton, P. (2019). Meridional oceanic heat transport influences marine heatwaves in the Tasman Sea on interannual to decadal timescales. *Frontiers in Marine Science, 6*, 228. https://www.frontiersin.org/articles/10.3389/fmars.2019.00228/abstract

https://fjfsdata01prod.blob.core.windows.net/articles/files/436714/pubmed-zip/.versions/1/.package-entries/fmars-06-00228/fmars-06-00228.pdf?sv=2015-12-11&sr=b&sig=imfNL%2Btj0DBN6jr%2F9J%2FKzkL5133CW%2ByD5LCId9PZyWg%3D&se=2019-09-05T10%3A06%3A24Z&sp=r&rscd=attachment%3B%20filename%2A%3DUTF-8%27%27fmars-06-00228.pdf

Behrens, E., Rickard, G., Morgenstern, O., Martin, T., Osprey, A., & Joshi, M. (2016). Southern Ocean deep convection in global climate models: A driver for variability of subpolar gyres and Drake Passage transport on decadal timescales. *Journal of Geophysical Research: Oceans, 121*(6), 3905--3925. http://doi.wiley.com/10.1002/2015JC011286

https://agupubs.onlinelibrary.wiley.com/doi/full/10.1002/2015JC011286

Behrens, E., Williams, J., Morgenstern, O., Sutton, P., Rickard, G., & Williams, M. J. M. (2020). Local Grid Refinement in New Zealand's Earth System Model: Tasman Sea Ocean Circulation Improvements and Super-Gyre Circulation Implications. *Journal of Advances in Modeling Earth Systems, 12*(7). <Go to ISI>://WOS:000556744300014

Blanke, B., & Raynaud, S. (1997). Kinematics of the Pacific Equatorial Undercurrent: An Eulerian and Lagrangian Approach from GCM Results. *Journal of Physical Oceanography, 27*(6), 1038--1053. http://dx.doi.org/10.1175 \% 2F1520-0485 \% 281997 \% 29027 \% 3C1038 \% 3AKOTPEU \% 3E2.0.CO \% 3B2 http://ams.allenpress.com/archive/1520-0485/27/6/pdf/i1520-0485-27-6-1038.pdf

Dagestad, K. F., Rohrs, J., Breivik, O., & Adlandsvik, B. (2018). OpenDrift v1.0: a generic framework for trajectory modelling. *Geoscientific Model Development, 11*(4), 1405-1420. <Go to ISI>://WOS:000429973800001

Debreu, L., Vouland, C., & Blayo, E. (2008). AGRIF: Adaptive grid refinement in Fortran. *Computers & Geosciences, 34*(1), 8-13. <Go to ISI>://WOS:000251657500002

Delandmeter, P., & van Sebille, E. (2019). The Parcels v2.0 Lagrangian framework: new field interpolation schemes. *Geosci. Model Dev., 12*(8), 3571-3584. https://gmd.copernicus.org/articles/12/3571/2019/

Döös, K., Jonsson, B., & Kjellsson, J. (2017). Evaluation of oceanic and atmospheric trajectory schemes in the TRACMASS trajectory model v6.0. *Geoscientific Model Development, 10*(4), 1733-1749. <Go to ISI>://WOS:000399918900001

Good, S. A., Martin, M. J., & Rayner, N. A. (2013). EN4: Quality controlled ocean temperature and salinity profiles and monthly objective analyses with uncertainty estimates. *Journal of Geophysical Research: Oceans, 118*(12), 6704--6716. http://doi.wiley.com/10.1002/2013JC009067

https://agupubs.onlinelibrary.wiley.com/doi/full/10.1002/2013JC009067

Hanchet, S., Dunn, A., Parker, S., Horn, P., Stevens, D., & Mormede, S. (2015). The Antarctic toothfish (Dissostichus mawsoni): biology, ecology, and life history in the Ross Sea region. *Hydrobiologia, 761*(1), 397-414. <Go to ISI>://WOS:000362964400023

Hanchet, S. M., Rickard, G. J., Fenaughty, J. M., Dunn, A., Williams, M. J. H., Hanchet, S. M., et al. (2008). A hypothetical life cycle for Antarctic toothfish (Dissostichus mawsoni) in the Ross See region. *CCAMLR Science, 15*, 35--53. http://archive.ccamlr.org/ccamlr _ science/Vol-15-2008/02hanchet-et-al.pdf

Kwok, R., & Morison, J. (2015). Sea surface height and dynamic topography of the ice-covered oceans from CryoSat-2: 2011-2014. *Journal of Geophysical Research: Oceans, 121*(1), n/a--n/a. http://doi.wiley.com/10.1002/2015JC011357

https://agupubs.onlinelibrary.wiley.com/doi/full/10.1002/2015JC011357

La Mesa, M. (2007). The utility of otolith microstructure in determining the timing and position of the first annulus in juvenile Antarctic toothfish (Dissostichus mawsoni) from the South Shetland Islands. *Polar Biology, 30*(10), 1219-1226.

Madec, G., Bourdallé-Badie, R., Bouttier, P.-A., Bricaud, C., Bruciaferri, D., Calvert, D., et al. (2017). NEMO ocean engine.

Meijers, A. J. S. (2014). The Southern Ocean in the Coupled Model Intercomparison Project phase 5. *Philosophical transactions. Series A, Mathematical, physical, and engineering sciences, 372*(2019), 20130296. http://classic.rsta.royalsocietypublishing.org/content/372/2019/20130296.full

Parker, S., & Di Blasi, D. (2020). Second winter survey of Antarctic toothfish (Dissostichus mawsoni) in the Ross Sea region. *Commission for the Conservation of Antarctic Marine Living Resources, SC-CAMLR-39/BG/29*.

Parker, S. J., Stevens, D. W., Ghigliotti, L., La Mesa, M., Di Blasi, D., & Vacchi, M. (2019). Winter spawning of Antarctic toothfish Dissostichus mawsoni in the Ross Sea region. *Antarctic Science, 31*(5), 243-253. <Go to ISI>://WOS:000508355900003

Roberts, J. O. (2012). Ecology and management of range edge populations: the case of toothfish species at the South Sandwich Islands.

Shaffrey, L., Stevens, I., Norton, W., Roberts, M., Vidale, P.-L., Harle, J., et al. (2009). UK HiGEM: The new UK high-resolution global environment model—Model description and basic evaluation. *Journal of Climate, 22*(8), 1861-1896.

Tsujino, H., Urakawa, S., Nakano, H., Small, R. J., Kim, W. M., Yeager, S. G., et al. (2018). JRA-55 based surface dataset for driving ocean–sea-ice models (JRA55-do). *Ocean Modelling, 130*, 79-139. https://www.sciencedirect.com/science/article/pii/S146350031830235X?via \% 3Dihub